

Quantitative nanoscale modulus measurements and elastic imaging of SnO₂ nanobelts

Yuegui Zheng and Robert E. Geer^{a)}

College of Nanoscale Science and Engineering, University at Albany, SUNY, Albany, New York 12203

Katharine Dovidenko

General Electric Global Research Center, Niskayuna, New York 12309

Malgorzata Kopycinska-Müller and Donna C. Hurley

National Institute of Standards and Technology, Boulder, Colorado 80305

(Received 6 July 2006; accepted 30 September 2006; published online 21 December 2006)

A comparative study of the elastic modulus and uniformity of single-crystal SnO₂ nanobelts is presented employing two nondestructive techniques based on atomic force microscopy: differential ultrasonic force microscopy (d-UFM) and atomic force acoustic microscopy (AFAM). In mapping mode both techniques revealed a uniform elastic response across the surface of the nanobelts as expected for single-crystal nanostructures. Comparative analyses of the local indentation modulus (probe area $\approx 100\text{--}400\text{ nm}^2$) were undertaken using both techniques at multiple points on the same SnO₂ nanobelt exhibiting a (102) surface crystalline orientation as determined by electron backscatter diffraction. Both d-UFM and AFAM exhibited excellent quantitative agreement yielding indentation moduli of 151 ± 14 and 154 ± 18 GPa, respectively. These values are significantly below the expected value of the (102) indentation modulus of 358 GPa for crystalline SnO₂ determined from the Green's function model of Barnett and Lothe [Phys. Nors. **8**, 13 (1975)] adapted by Vlassak *et al.* [J. Mech. Phys. Solids **51**, 1701 (2003)]. This observation is consistent with recent nanoindentation (destructive) measurements of (10 $\bar{1}$) oriented SnO₂ nanobelts that yielded an indentation modulus of 66 ± 10 GPa, well below the expected value of 308 GPa. In addition to confirming the quantitative consistency and overall accuracy of nanoscale modulus measurements using d-UFM and AFAM, the overall trend in these data contradicts recent molecular dynamics studies that call for increased elastic moduli in similar nanobelt structures. © 2006 American Institute of Physics. [DOI: 10.1063/1.2401027]

INTRODUCTION

Since the work of Iijima on carbon nanotubes a wide variety of single-crystal, quasi-one-dimensional nanostructures has been reported including non-carbon-based nanotubes and so-called nanowires or nanobelts.^{1–6} These nanomaterials exhibit a variety of unique morphologies that hold promise for improved functionality as engineered components for nanoscale materials or devices. Still, the relevant length scales associated with these structures present significant challenges in fundamental material analysis and investigation necessary for practical application. A case in point is the quantitative measurement of local elastic properties of such structures. Although nanoindentation has been widely used as a tool for local measurement of indentation modulus it is an inherently destructive technique inducing significant local plastic deformation.⁷ It likewise lacks nanoscale-resolved mapping capability. In contrast, the combination of ultrasonic actuation with scanning probe microscopy (SPM) over the past decade has enabled quantitative extraction of local surface elastic properties in addition to the nanoscale mapping of mechanical variations.^{8–12}

Here, we report the application of two such techniques, differential ultrasonic force microscopy (d-UFM) and atomic

force acoustic microscopy (AFAM), to investigate the local nanomechanical properties of single-crystal SnO₂ nanobelts. The motivation is twofold. Firstly, the chemical stability and single-crystal and geometrically regular morphologies of these structures constitute an ideal platform for comparative analyses of ultrasonic nanomechanical characterization techniques based on scanning probe microscopy for purposes of nanoscale mapping and quantitative extraction of local indentation modulus. Secondly, recent nanoindentation-based modulus measurements of single-crystal SnO₂ nanobelts reported by Zhao *et al.*, show a 75% reduction in elastic constants compared to bulk tetragonal (rutile) SnO₂.^{13,14} This observation counters recent molecular dynamics studies by Kulkarni *et al.* for similar semiconducting oxide (ZnO) nanobelts which predict that the elastic modulus increases with decreasing size.¹⁵ This effect is most pronounced for nanobelts with relatively small cross-sectional dimensions (~ 4 nm and below) and originates from internal compressive stress induced by surface stresses resulting from reconstruction of surface Zn and O atoms. In order to study the unexpected modulus reduction of these materials and the apparent disagreement with theoretical modeling we investigated samples that we believe to be without known mechanisms for modulus reduction for investigation via d-UFM and AFAM.

^{a)}Electronic mail: rgeer@uamail.albany.edu

The remainder of the paper is organized as follows. The following section describes SnO₂ nanobelt synthesis, compositional characterization, crystallographic characterization, and structure fabrication for nanomechanical testing. In addition, experimental descriptions and testing protocols are outlined for both d-UFM and AFAM. Experimental results are then presented for the nanobelt morphology, composition, and crystal orientation followed by d-UFM force-deflection data analysis and AFAM flexural resonance data analysis. These data are discussed with respect to modeling results based on the adaptation of Vlassak *et al.* of Barnett and Lothe's Green's function model for the calculation of the indentation modulus from anisotropic elastic media¹⁶ and compared to recent nanoindentation data from (10 $\bar{1}$) oriented SnO₂ nanobelts and recent molecular dynamics modeling.

EXPERIMENT

SnO₂ nanobelts were synthesized following the procedure outlined in Ref. 6. Tin powder was placed in a crucible within a quartz tube furnace. The reaction chamber was heated to 800 °C under an Ar/O₂ flow and maintained at that temperature for 2 h followed by a cooling ramp to room temperature. The deposited material was removed from alumina substrates adjacent to the crucible in the oven and dispersed in a solvent (acetone or ethanol) for solvent-based deposition on Si (001) substrates. SnO₂ nanobelts deposited on Si (001) substrates were mounted in a focused ion beam scanning electron microscope (FIB-SEM) where fiducial markings were ion milled to reproducibly locate nanobelts of interest. SnO₂ nanobelts undergoing nanomechanical imaging and modulus extraction were immobilized on the Si substrate through ion-beam assisted deposition of Pt at the ends of the nanobelt in the FIB-SEM. For purposes of mechanical measurements the nanobelts are considered bonded to the substrate. This assumption was validated through analyses of multiple contact topographic images on two separate AFM systems which showed no relative nanobelt displacements. Care was taken to perform all subsequent compositional, topographical, and mechanical testings on areas of the nanobelts sufficiently removed from the deposited Pt to avoid effects of ion exposure.

The SEM of SnO₂ nanobelts utilized a Zeiss 1550 SEM. Auger electron spectroscopy (AES) was carried out to characterize compositional uniformity of the nanobelts using a scanning Auger multiprobe spectrometer with a 5 keV primary electron beam with an elemental sensitivity of 1%. AES depth profiling employed a 4 keV Ar-ion sputter beam. The AES probe beam diameter was approximately 1 μ m. Electron backscatter diffraction (EBSD) was employed to determine the crystal orientation of the surface plane of SnO₂ nanobelt samples using a dual-beam FIB-SEM. The analysis of EBSD patterns for SnO₂ nanobelts utilized a Si (001) calibration standard.

Ultrasonic force microscopy and topography image scans utilized a commercial atomic force microscope (AFM). The experimental configuration has been reported.^{17,18} A 2.7 kHz modulated ultrasonic vibration (\sim 2 MHz) is applied to the sample in contact with the scanning tip (commercial

Si₃N₄ cantilever with a spring constant \sim 0.5 N/m and nominal tip radius of 20 nm). At a threshold vibration amplitude the tip-sample force varies nonlinearly with the tip-sample displacement resulting in a quasistatic tip deflection related directly to the tip-sample mechanics.¹⁹ The resulting UFM image contrast increases monotonically with the sample contact stiffness (neglecting local variations in the tip-sample adhesion). Quantitative calibration and extraction of the surface indentation modulus employed the d-UFM technique developed by Dinelli *et al.*^{9,20} wherein vibration amplitude sweeps were carried out as a function of the applied tip force to reconstruct the quasistatic tip-sample force-distance curve. Typical applied tip forces ranged from 25 to 125 nN. For d-UFM a very small scan size (10 \times 10 nm²) is used during the force-distance data acquisition to avoid artifacts associated with local, tip-induced surface modification. Six sites within a 1 μ m² region on the SnO₂ nanobelt were evaluated via d-UFM at several frequencies near 2 MHz. Multiple frequencies were sampled to confirm the absence of cantilever resonances which can complicate the force curve extraction in d-UFM. Calibration measurements for the d-UFM indentation modulus extraction were acquired from the Si (001) substrate (indentation modulus of 165 GPa). All calibration measurements were acquired within approximately 1 μ m of the SnO₂ test sites to ensure uniformity of the piezoinduced ultrasonic vibration amplitude. Six Si (001) sites were sampled at several frequencies near 2 MHz to confirm the absence of resonance effects. A Hertzian contact model was used for the determination of the sample indentation modulus.^{9,20}

In contrast to d-UFM, AFAM actively exploits the resonant frequencies of the cantilever to extract the local sample indentation modulus.^{10,11} When the cantilever tip is in contact with a sample surface, the resonant frequencies shift relative to the values for a free-space cantilevered tip. By measuring the free and contact-resonance frequencies, the indentation modulus of the sample can be extracted. For the data shown below, a commercial SPM system was configured for AFAM operation.¹¹ A rectangular, single-crystal Si cantilever with a spring constant $k_c \approx$ 40 N/m is used. At each position on the sample, resonant spectra are acquired for the lowest three flexural resonant modes of the cantilever at three different values of the cantilever deflection δ . Given the relation $F_N = k_c \delta$ between the deflection and the applied force F_N , the experimental values of $\delta =$ 15, 30, and 45 nm correspond to applied forces between 0.6 and 1.8 μ N for the work reported here. Contact-resonance measurements are made on the Si substrate and the SnO₂ nanobelt in alternation using the same values of δ . From the experimental resonant frequencies, values are calculated for the tip-sample contact stiffness for both the test (SnO₂) and reference (Si) materials. The values of the contact stiffness for the test and reference samples are compared in order to obtain the desired quantity, the indentation modulus of the test sample, utilizing a Hertzian contact model.¹¹ For imaging, the contact resonance frequency is acquired through a custom circuit based on a 32 bit floating-point digital signal processor.¹² By feeding back the contact-resonance frequency to the SPM controller, a "frequency-tracking" image is acquired for a specific reso-

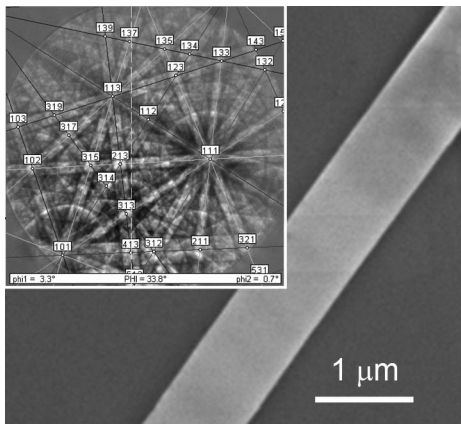


FIG. 1. Scanning electron micrograph of a (102) SnO₂ nanobelt pinned to a Si (001) substrate for nanomechanical investigation. Inset: Electron backscatter diffraction image used to determine the crystalline orientation of the nanobelt.

nant mode across the nanobelt surface. An AFAM indentation modulus map is achieved by calculating the indentation modulus at each pixel from the frequency images using conventional AFAM analysis methods and assuming Hertzian contact mechanics.

RESULTS

The morphology of the nanobelts was characterized via SEM and contact mode AFM. The crystalline orientation was determined via EBSD. Figure 1 displays a SEM micrograph of the SnO₂ nanobelt investigated for this work. Figure 2 displays an AFM topograph of the same region of the nanobelt. The overall nanobelt length was approximately 60 μm. The average width and height of the nanobelt were 901 ± 10 and 44 ± 8 nm, respectively. The nanobelt surface was atomically smooth with a root-mean-square (RMS) roughness of 0.42 nm. The crystal orientation was determined from the EBSD pattern (inset Fig. 1). Utilizing the Si (001) substrate as a calibration constant, analysis of the EBSD pattern revealed the expected tetragonal crystal structure ($a=b=0.475$ nm, $c=0.32$ nm, and $\alpha=\beta=\gamma=90^\circ$) for single-crystal, stoichiometric SnO₂ (O: 66.7 at. %, Sn: 33.3 at. %).²¹ The lattice constants and elemental composition are in agreement with earlier investigations of nanobelts exhibiting other crystalline orientations reported by our

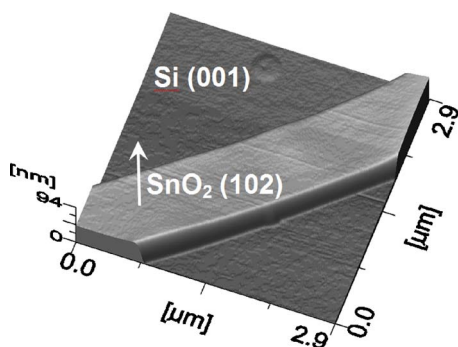


FIG. 2. Three-dimensional topographic image of the SnO₂ nanobelt pictured in Fig. 1 acquired via contact-mode atomic force microscopy. The crystalline orientation of the nanobelt is labeled.

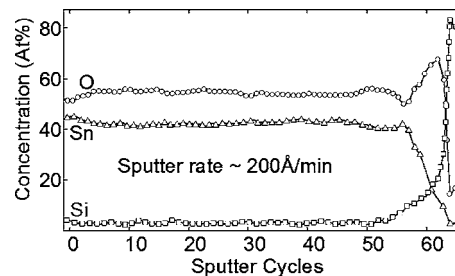


FIG. 3. Elemental depth profile acquired via AES on the SnO₂ nanobelt shown in Figs. 1 and 2. The elemental composition is uniform throughout the nanobelt. The Si contribution originates from the substrate.

group using transmission electron beam diffraction.²² The surface normal of the SnO₂ nanobelt pictured in Figs. 1 and 2 is parallel to the (102) reciprocal lattice vector.

To confirm the compositional uniformity of the nanobelt, AES sputter profiling was carried out. The results are shown in Fig. 3. The Auger spectrometer primary electron beam diameter is slightly larger than the nanobelt resulting in a small Si signal from the substrate. Discounting this, AES profiling yielded a compositionally uniform nanobelt free from impurities to within the sensitivity of the instrument. Nominal AES elemental sensitivity coefficients were used for the spectra in Fig. 3 and are responsible for the apparent nonstoichiometric O/Sn ratio. The raw data are shown as collected and have not been recalibrated or renormalized. The aforementioned EBSD data, electron diffraction data,²² confirm an O/Sn elemental ratio of 2/1 for all nanobelts studied. There are no indications from any of the structural, compositional, or elastic characterization approaches discussed above or published previously by our group²² that the single-crystal SnO₂ nanobelts differ in any respects from bulk SnO₂ in terms of porosity, stoichiometric ratio, or average density.

UFM imaging (Fig. 4) of the SnO₂ nanobelt was carried out simultaneously with the AFM contact mode imaging shown in Fig. 2. With the exception of anomalous features corresponding to the tip contact with the nanobelt edges the UFM contrast across the nanobelt is uniform (0.17 ± 0.005 V). The UFM contrast of the nanobelt is strikingly similar to that of the Si (001) substrate indicating similar surface contact stiffnesses. For a quantitative determination of the local surface contact stiffness and indentation

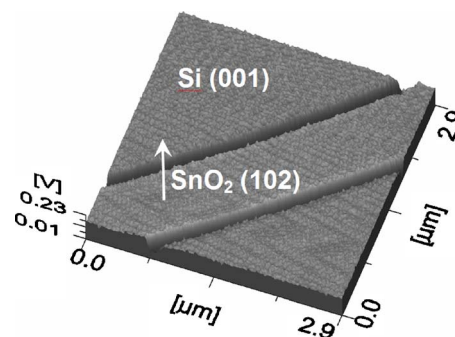


FIG. 4. Ultrasonic force microscopy image of the SnO₂ nanobelt shown in Figs. 1 and 2. The UFM contrast is uniform across the nanobelt and strikingly similar to the Si (100) substrate.

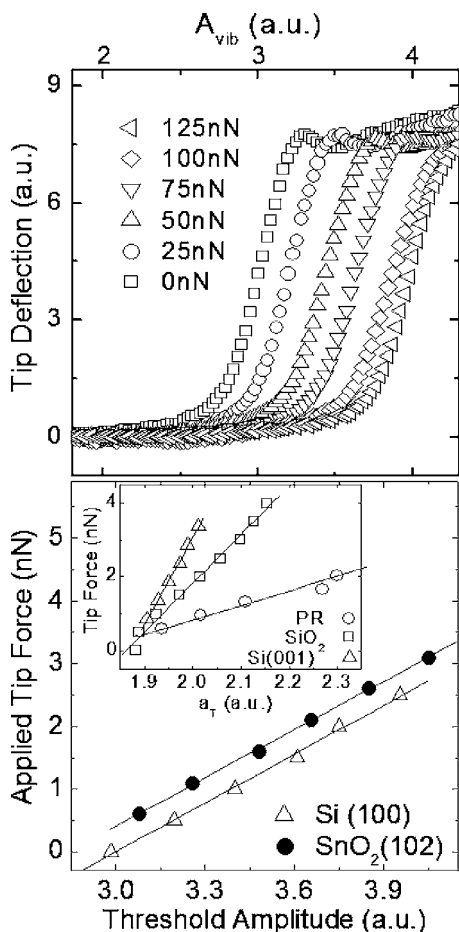


FIG. 5. Upper graph: Plots of the average UFM tip deflection as a function of the vibration amplitude for increasing applied tip force to illustrate the determination of the threshold amplitude (taken as the inflection point). Lower graph: Plot of the applied tip force vs ultrasonic vibration threshold amplitude acquired at a single point on the (102) SnO_2 nanobelt (filled circles) and Si (001) substrate (open triangles). A linear relationship is observed, the slope of which corresponds to the surface contact stiffness (Ref. 22). The upper left insert to this graph shows the applied tip force vs threshold amplitude for Si (001), SiO_2 , and cured photoresist to illustrate relative sensitivity of d-UFM to variations in surface contact stiffness.

modulus, d-UFM analysis was carried out at several sites on the SnO_2 nanobelt. As noted above, this entails extraction of the surface contact stiffness through the measurement of the UFM threshold amplitude as a function of the applied tip force. The variation of the UFM threshold vibration amplitude with the applied tip force from a single point on the SnO_2 nanobelt is shown in the upper inset in Fig. 5. The open symbols in the inset denote the quasistatic tip deflection as a function of the linearly increasing vibration amplitude. The threshold is determined as the point of the maximum slope of the tip deflection curve. The sudden variation in this slope with increasing vibration amplitude reflects the “pull off” of the tip from the nanobelt surface which is directly related to its elastic properties.^{8,9,20} This relationship is plotted as a function of the threshold amplitude in Fig. 5 acquired at a single point on the SnO_2 (102) and Si (001) surfaces. The slopes of these curves represent the surface contact stiffness of the two materials. The two curves are offset from one another for clarity.

The average ratio of the SnO_2 (102) surface contact stiff-

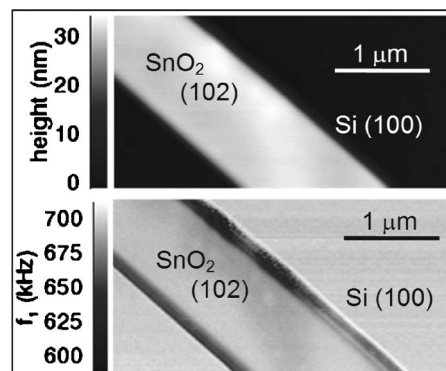


FIG. 6. Two-dimensional scans of surface topography (top) and first-order cantilever flexural resonance (bottom) of the SnO_2 nanobelt shown in Figs. 1 and 2.

ness to the Si (001) surface contact stiffness from d-UFM is 0.96 ± 0.06 . This ratio represents data acquired at six points on the nanobelt and six points on the Si substrate which required the acquisition of 144 separate data sets detailing the variation of the UFM threshold amplitude with the applied tip force and ultrasonic frequency. The similarity between the contact stiffness of the SnO_2 (102) surface and the Si (001) surface is unexpected. For purposes of comparison and documentation of the relative sensitivity of d-UFM to changes in surface contact stiffness, the lower inset in Fig. 5 plots the applied tip-force versus UFM threshold amplitude (a_T) for three separate materials: fully cured photoresist, SiO_2 deposited via plasma-enhanced chemical vapor deposition of tetraethylorthosilicate, and Si (001). As with the data in the main portion of the figure the slopes of these three data sets correspond to relative surface contact stiffness. These data and data previously published on silicon nitride and silicon oxide confirm the ability of d-UFM to differentiate materials on the basis of surface contact stiffness and documents for the current work that the SnO_2 nanobelt contact stiffness is unexpectedly similar to that of the Si (001) substrate.²⁰

The indentation modulus of the Si (001) surface is 165 ± 15 GPa.^{23–25} Employing a Hertzian contact model for the tip/sample interaction for the d-UFM data and taking the Young’s modulus and Poisson’s ratio of the Si_3N_4 tip to be 310 ± 25 GPa and 0.23 ± 0.02 , respectively, the measured indentation modulus of the SnO_2 (102) nanobelt is 151 ± 14 GPa.

A similar analysis of the surface elastic properties of the SnO_2 nanobelt was carried out via AFAM. Simultaneous topographic and AFAM imaging scans are shown in Fig. 6. The upper panel displays a nanobelt topography image, while the lower panel of Fig. 6 shows image data corresponding to spatial variation in the first flexural resonance of the AFAM cantilever. The applied AFAM tip load used for these data was 600 nN. The cantilever flexural resonance image scan shows very little contrast between the Si (001) substrate and the nanobelt surface with the exception of the nanobelt edges where rapid changes in the tip-sample contact area occur during scanning. This implies that the surface elastic properties of the SnO_2 nanobelt are extremely similar to the Si substrate, in qualitative agreement with the UFM

image of Fig. 4. For a quantitative comparison between resonant and d-UFM analyses of the nanobelt, point measurements of the indentation modulus were carried out via AFAM following the protocol outlined above. Measurements were made at four different positions on the SnO₂ nanobelt and five positions on the Si substrate. At each point, the contact-resonance frequencies of the three lowest flexural modes were determined for three values of the cantilever deflection δ as described above. Each set of nanobelt measurements was compared to the corresponding Si data acquired immediately beforehand and afterwards. Including all possible combinations of mode pairs, this provided a total of 63 contact stiffness ratios from which the indentation modulus was determined. Employing the data analysis approach reported in Ref. 11 and assuming Hertzian contact mechanics, a value of 154 ± 18 GPa for the surface indentation modulus of the SnO₂ nanobelt was obtained with AFAM. This is in excellent agreement with the d-UFM data discussed above. The AFAM analysis provides an independent confirmation of the d-UFM results and directly supports the experimental observations noted above.

DISCUSSION

Both AFAM and d-UFM techniques utilize the approximately spherical tip of a SPM cantilever to nondestructively probe the SnO₂ nanobelt surface albeit in different modes. AFAM monitors the resonance frequency of the cantilever to characterize frequency shifts due to the elastic coupling between the cantilever and the sample surface, i.e., it is an inherently dynamic technique. In contrast, d-UFM purposely avoids resonance frequencies in order to exploit the inertial damping of the cantilever to probe the elastic properties of the sample surface through the characterization of the quasi-static deflection of the tip that results from the nonlinear dependence of the tip-sample force as a function of the elastic indentation depth. The quantitative agreement between the AFAM and d-UFM techniques in determining the surface contact stiffness and indentation modulus of the (102) surface of the SnO₂ nanobelt sample is not unexpected since both approaches exploit the interaction of the tip with the sample surface to carry out the modulus measurement. However, the independent agreement of the two methods strongly supports the quantitative accuracy of both. Coupled with earlier and similar works using both techniques the present work affirms their quantitative capabilities.^{9–12,20}

The finite thickness of the nanobelt is not expected to have a dramatic effect on the d-UFM measurements due to the relatively low tip forces employed. For a spherical tip contacting a planar surface the stress field penetrates to a depth of roughly $3a$, where a is the tip-sample contact radius.²⁶ Based on the d-UFM experimental parameters, force range probe depths of 14–24 nm are estimated, well below the measured thickness of the nanobelt. For AFAM the same Hertzian contact mechanics applies and the stress field penetration is estimated to be 45–60 nm. The upper bound for the AFAM probe depth exceeds the measured nanobelt thickness indicating a possible contribution from the Si substrate. If such were the case it would imply an even lower

value for the nanobelt modulus than was actually measured via AFAM. However, since the d-UFM results and the AFAM results agree very well we conclude that the effect of the substrate contribution to the AFAM measurement is not substantial.

The agreement between the AFAM and d-UFM indentation modulus data provides confidence on their joint accuracy for comparison with other approaches. Recent studies on SnO₂ nanobelts with similar morphologies have been carried out by Zhao *et al.* using nanoindentation.¹⁴ The authors of that work characterized the mechanical properties of a SnO₂ nanobelt with a (10 $\bar{1}$) surface orientation and reported an indentation modulus of 66 ± 10 GPa. A quantitative comparison with the present work requires consideration of the crystal orientation. Based on reported measurements of the bulk elastic constants of SnO₂ by Chang and Graham, the Young's moduli along the (10 $\bar{1}$) and (102) directions in a tetragonal (rutile) SnO₂ crystal are 265 and 317 GPa, respectively.²⁷ For isotropic materials the indentation modulus can be easily calculated from the Young's modulus and Poisson's ratio. However, this is not possible for anisotropic materials. However, Vlassak *et al.* have developed an effective approximation for calculating the indentation modulus for anisotropic materials.¹⁶ This approach is based on the Green's function model of Barnett and Lothe.²⁸ Briefly, that approach, based on the Stroh formalism, employs a Rayleigh-Ritz approximation for the tip-sample contact area that maximizes the indentation force. This provides a pathway for approximating the indentation modulus for the SnO₂ nanobelts along the surface crystal orientations of interest.

Following this approach the indentation moduli for the (10 $\bar{1}$) and (102) surfaces of a tetragonal (rutile) SnO₂ nanobelt were calculated to be 308 and 358 GPa, respectively. The respective increases in comparison to the Young's modulus arise from contributions made by the larger elements of the elastic constant matrix. Both the approximation of the indentation moduli and the Young's moduli along the (10 $\bar{1}$) and (102) directions are substantially larger than the measured values presented here and in Ref. 14. Although a detailed experimental comparison between d-UFM, AFAM, and nanoindentation has yet to be carried out, the experimentally observed trend of dramatically reduced indentation moduli of SnO₂ nanobelts is consistent among all three approaches.

It is important to note that the absolute accuracy of AFAM, and to a similar extent d-UFM, is optimal if the modulus of the reference materials used is close (within perhaps $\pm 20\%$) to that of the test material. Reference materials above or below this range will result in an over- or underestimation of the sample indentation modulus. Consequently, if the SnO₂ nanobelt modulus was in the 300–350 GPa range, as predicted from bulk SnO₂ elastic constants, one would extract a lower value in AFAM measurements using Si with $M \sim 165$ GPa as a reference. However, it is clear that this circumstance is not responsible for the experimental observations since the measured contact stiffness of the nanobelts is close to, and *lower*, than that of the Si.

There are no experimental or theoretical results which

account for the low values of the SnO₂ nanobelt indentation modulus presented above or described in Ref. 14. On the contrary, recent molecular dynamics studies published by Kulkarni *et al.* for ZnO nanobelts predict that the elastic modulus increases with decreasing size.¹⁵ This effect is most pronounced for nanobelts with relatively small cross-sectional dimensions (~4 nm and below) and originates from the internal compressive stress induced by surface stresses resulting from the reconstruction of surface Zn and O atoms. Although surface atom reconstruction may certainly differ for the tin-oxide nanobelt system resulting in quantitative variations with respect to ZnO nanobelts, the surface-induced stress model is not expected to lower the elastic moduli of SnO₂ nanobelts. Moreover, the modeling results predict that these finite-size effects become minimal at cross-sectional length scales similar to those of the nanobelts studied for the present work. Consequently, it is concluded that the finite-size effects described in the modeling work of Ref. 15 are not evident for the structures studied here and that the anomalously low indentation modulus is not directly attributable to those effects.

As noted above there are no indications from any of the structural, compositional, or elastic characterization approaches presented here that the single-crystal SnO₂ nanobelts differ in any respects from bulk SnO₂ in terms of porosity, stoichiometric ratio, or average density—the most likely origins for modulus reduction. And since d-UFM, AFAM, and nanoindentation all have measured anomalously low indentation moduli for SnO₂ nanobelts it is not possible to attribute the results to experimental artifacts. Continued theoretical and experimental investigations of these materials are, hence, necessary to investigate finite-size effects with respect to nanoscale mechanical properties in these self-assembled systems.

CONCLUSION

We report the application of differential ultrasonic force microscopy and atomic force acoustic microscopy to investigate the local nanomechanical properties of single-crystal SnO₂ nanobelts. Both AFAM and d-UFM were employed for imaging and local quantitative modulus measurements on the same SnO₂ nanobelt. Both techniques yielded a uniform elastic response over the imaged area. Quantitative extraction of the local indentation modulus (~100–400 nm² probe area) yielded values of 151±14 GPa (d-UFM) and 154±18 GPa (AFAM). These values are significantly below the expected value for the (102) indentation modulus of 358 GPa for the crystalline SnO₂ determined from the Green's function model of Barnett and Lothe adapted by Vlassak *et al.* This observation is consistent with recent nanoindentation (destructive) measurements of (101̄) ori-

ented SnO₂ nanobelts that yielded an indentation modulus of 66±10 GPa, well below the expected value of 308 GPa, and contradict recent molecular dynamics studies that call for increased elastic moduli in similar nanobelt structures.

ACKNOWLEDGMENTS

The authors gratefully acknowledge the support from the Microelectronics Advanced Research Corporation, the New York State Office of Technology and Academic Research, and the National Science Foundation (Grant Nos. DMR-0320569 and DMR-0303764). It is a pleasure to acknowledge Pulickel Ajayan for assistance with nanobelt samples.

¹S. Iijima, *Nature (London)* **354**, 56 (1991).

²L. Vaccarini, C. Goze, L. Henrard, E. Hernandez, P. Bernier, and A. Rubio, *Carbon* **38**, 1681 (2000).

³Y. Wu, J. Xiang, C. Yang, W. Lu, and C. M. Lieber, *Nature (London)* **430**, 61 (2004).

⁴Z. W. Pan, Z. R. Dai, and Z. L. Wang, *Science* **291**, 1947 (2001).

⁵E. Comini, G. Faglia, G. Sberveglieri, Z. Pan, and Z. L. Wang, *Appl. Phys. Lett.* **81**, 1869 (2002).

⁶S. H. Sun, G. W. Meng, Y. W. Wang, T. Gao, M. G. Zhang, Y. T. Tian, X. S. Peng, and L. D. Zhang, *Appl. Phys. A: Mater. Sci. Process.* **A76**, 287 (2003).

⁷A. C. Fischer-Cripps, *Nanoindentation* (Springer, New York, 2002), pp. 21–36.

⁸K. Yamanaka, H. Ogiso, and O. Kolosov, *Appl. Phys. Lett.* **64**, 178 (1994).

⁹F. Dinelli, S. K. Biswas, G. A. D. Briggs, and O. V. Kolosov, *Phys. Rev. B* **61**, 13995 (2000).

¹⁰U. Rabe and W. Arnold, *Appl. Phys. Lett.* **64**, 21 (1994); U. Rabe, M. Kopycinska, S. Hirsekorn, J. Muñoz Saldaña, G. A. Schneider, and W. Arnold, *J. Phys. D* **35**, 2621 (2002).

¹¹D. C. Hurley, K. Shen, N. M. Jennett, and J. A. Turner, *J. Appl. Phys.* **94**, 2347 (2003).

¹²D. C. Hurley, M. Kopycinska-Müller, A. B. Kos, and R. H. Geiss, *Meas. Sci. Technol.* **16**, 2167 (2005).

¹³S. X. Mao, M. Zhao, and Z. L. Wang, *Appl. Phys. Lett.* **83**, 993 (2003).

¹⁴M. Zhao, C. Jiang, S. Li, and S. X. Mao, *Mater. Sci. Eng., A* **409**, 223 (2005).

¹⁵A. J. Kulkarni, M. Zhou, and F. J. Ke, *Nanotechnology* **16**, 2749 (2005).

¹⁶J. Vlassak, M. Ciavarella, J. R. Barber, and X. Wang, *J. Mech. Phys. Solids* **51**, 1701 (2003).

¹⁷O. Kolosov and K. Yamanaka, *Jpn. J. Appl. Phys., Part 2* **32**, L1095 (1993).

¹⁸G. S. Shekhawat, O. V. Kolosov, G. A. D. Briggs, and R. E. Geer, *J. Appl. Phys.* **91**, 4549 (2002).

¹⁹F. Dinelli, M. R. Castell, D. A. Ritchies, N. J. Mason, G. A. D. Briggs, and O. V. Kolosov, *Philos. Mag. A* **80**, 2299 (2000).

²⁰L. Muthuswami and R. E. Geer, *Appl. Phys. Lett.* **84**, 5082 (2004).

²¹S. R. Vishwakarma, J. P. Upadhyay, and H. C. Prasad, *Thin Solid Films* **176**, 99 (1989).

²²Y. Zheng and R. E. Geer, *Proc. SPIE* **5392**, 14 (2004).

²³G. Grimvall, *Thermophysical Properties of Materials* (Elsevier, New York, 1999).

²⁴H. J. McSkimin and P. A. Andreatch, *J. Appl. Phys.* **35**, 2161 (1964).

²⁵J. J. Vlassak and W. D. Nix, *Philos. Mag. A* **67**, 1045 (1993).

²⁶A. C. Fischer-Cripps, *Nanoindentation* (Springer, New York, 2002), pp. 71–72 and 100–103.

²⁷E. Chang and E. K. Graham, *J. Geophys. Res.* **80**, 2595 (1975).

²⁸D. M. Barnett and J. Lothe, *Phys. Norv.* **8**, 13 (1975).